JOURNAL OF SYNCHROTRON RADIATION

ISSN 1600-5775

The vacuum ultraviolet beamline/endstations at NSRL dedicated to combustion research

Zhongyue Zhou,[a,b]‡ Xuewei Du,[b]‡ Jiuzhong Yang,[b] Yizun Wang,[a,b] Chaoyang Li,[c] Shen Wei,[b] Liangliang Du,[b] Yuyang Li,[a,b] Fei Qi[a,b]* and Qiuping Wang[b]*

[a]School of Mechanical Engineering, Shanghai Jiao Tong University, Shanghai 200240, People's Republic of China, [b]National Synchrotron Radiation Laboratory, University of Science and Technology of China, Hefei, Anhui 230029, People's Republic of China, and [c]China Academy of Engineering Physics, Mianyang, Sichuan 621900, People's Republic of China. *Correspondence e-mail: fqi@sjtu.edu.cn, qiuping@ustc.edu.cn

Received 11 February 2016
Accepted 7 April 2016

Edited by J. F. van der Veen

‡ These authors contributed equally to this work.

Keywords: VUV beamline; combustion; premixed flame; flow reactor.

An undulator-based vacuum ultraviolet (VUV) beamline (BL03U), intended for combustion chemistry studies, has been constructed at the National Synchrotron Radiation Laboratory (NSRL) in Hefei, China. The beamline is connected to the newly upgraded Hefei Light Source (HLS II), and could deliver photons in the 5–21 eV range, with a photon flux of 10^{13} photons s^{-1} at 10 eV when the beam current is 300 mA. The monochromator of the beamline is equipped with two gratings (200 lines mm^{-1} and 400 lines mm^{-1}) and its resolving power is 3900 at 7.3 eV for the 200 lines mm^{-1} grating and 4200 at 14.6 eV for the 400 lines mm^{-1} grating. The beamline serves three endstations which are designed for respective studies of premixed flame, fuel pyrolysis in flow reactor, and oxidation in jet-stirred reactor. Each endstation contains a reactor chamber, an ionization chamber where the molecular beam intersects with the VUV light, and a home-made reflectron time-of-flight mass spectrometer. The performance of the beamline and endstations with some preliminary results is presented here. The ability to detect reactive intermediates (*e.g.* H, O, OH and hydroperoxides) is advantageous in combustion chemistry research.

1. Introduction

The need to control pollutant emissions from the combustion of fossil fuels motivates interest in understanding these processes. Combustion phenomena are basically chemical processes with rapid heat production (Emmons, 1971). Thousands of reactions and intermediates are involved in the combustion of practical fuels. Understanding complex chemical reaction processes largely depends on accurate qualitative and quantitative information regarding the intermediates involved (Buckmaster *et al.*, 2005; Miller *et al.*, 2005; Westbrook *et al.*, 2005). Thus, direct measurements of these key species are critically important. However, detection of ideally all intermediates (stable or unstable) with modern analytical instruments is no walk in the park, because even the reaction networks of a simple fuel with a single component may contain hundreds of species with concentrations varying from several percent to trace level. The aforementioned challenges motivated the development of a sensitive experimental approach with universal detecting capability.

Synchrotron-based vacuum ultraviolet (VUV) photoionization mass spectrometry (PIMS) is sensitive and has proven to be a powerful approach for chemical kinetic studies of combustion (Hansen *et al.*, 2009; Qi, 2013) attributing to utilizing the molecular beam sampling and the tunability of the VUV light over a broad energy range.

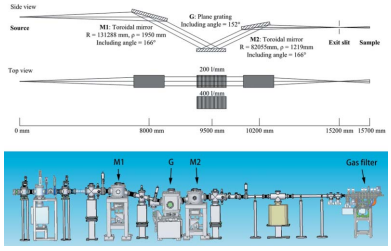

The molecular beam sampling system is used to extract sampled gases with a free-jet rapid expansion, in which the sampled molecules are 'frozen' as the jet reaches a collisionless free-molecular flow (Kantrowitz & Grey, 1951; Anderson & Fenn, 1965; Smalley *et al.*, 1977; Campargue, 1984; Zhan *et al.*, 1998; Guan *et al.*, 2014). Thus, mass spectrometers with molecular beam sampling systems are capable of measuring reaction intermediates such as short-lived radicals that are imperceptible to other diagnostic techniques (*e.g.* gas chromatography).

As shown in Fig. 1, the ionization energies (IEs) of most organic molecules are in the range 8–13 eV. Synchrotron light sources can produce tunable and intense VUV light in this range, and make it possible to achieve near-threshold photoionization of molecules without fragmentation. Moreover, the isomers can be distinguished based on their different ionization energies by scanning their photoionization efficiency (PIE) spectra (Cool, McIlroy *et al.*, 2005; Qi & McIlroy, 2005; Qi *et al.*, 2006). The application of the molecular beam mass spectrometry with synchrotron VUV photoionization technique has achieved great success in this area, presenting sensitive and comprehensive measurements of components in combustion studies (Taatjes *et al.*, 2005; Battin-Leclerc *et al.*, 2010).

Synchrotron-based VUV PIMS for combustion chemistry was firstly utilized at the Advanced Light Source of Lawrence Berkeley National Laboratory, USA (Heimann *et al.*, 1997; Cool, McIlroy *et al.*, 2005) and the National Synchrotron Radiation Laboratory (NSRL) in Hefei, China (Qi *et al.*, 2006; Zhou *et al.*, 2013). Very recently photoionization-based photoelectron photoion coincidence (PEPICO) spectroscopy has also been employed to investigate combustion at the Swiss Light Source (SLS) of the Paul Scherrer Institut in Switzerland (Johnson *et al.*, 2009; Oßwald *et al.*, 2014) and the SOLEIL synchrotron near Paris, France (Nahon *et al.*, 2012; Krüger *et al.*, 2014). The application of PEPICO makes it possible to clearly distinguish isomers with a difference of less than 30 meV in IE (Hemberger *et al.*, 2014). These facilities feature 'selective' and 'isomer-resolved' detection, attributable to the tunability of synchrotron VUV light, making them ideal platforms for experimental studies of combustion chemistry. Applications of the synchrotron-based VUV PIMS include premixed flames with McKenna burners, fuel pyrolysis in plug-flow reactors, oxidation in jet-stirred reactors, non-premixed co-flow flames, *etc*.

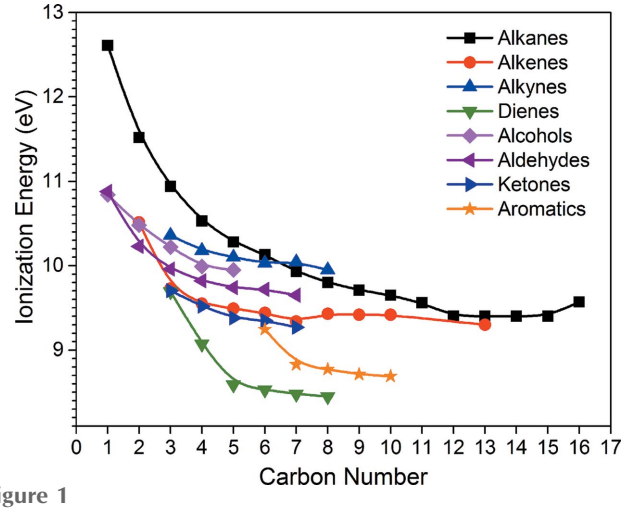

Figure 1
Ionization energies of some organic molecules (Photoionization Cross Section Database, 2011; Linstrom & Mallard, 2016).

The Hefei Light Source (HLS) at NSRL has been shut down for upgrade since May 2012. An undulator VUV beamline (BL03U) intended for combustion chemistry research has been constructed and brought into operation recently. The beamline serves three endstations which are designed for respective studies of premixed flames, fuel pyrolysis in flow reactors and oxidation in jet-stirred reactors. In the following sections, the VUV beamline and the three experimental endstations will be introduced in detail, with their performance demonstrated by some preliminary results.

2. VUV beamline

2.1. Light source and optical system

The upgraded HLS (HLS II) is operated at 800 MeV with a maximum beam current of 300 mA in decay mode, and the electron beam emittance is approximately 36 nm rad. A quasi-periodic undulator (Hwang *et al.*, 2002; Nahon & Alcaraz, 2004; Yang *et al.*, 2014) is used as the light source of the VUV beamline. The source size is approximately 0.76 mm (σ_h) × 0.1 mm (σ_v) and the emission angle is approximately 0.25–0.1 mrad (both σ_h' and σ_v') in the energy range from 5 to 21 eV. The beamline acceptance angle is designed as 1 mrad (horizontal) × 1 mrad (vertical).

Considering the light characteristics of the undulator, the center of the undulator is regarded as the source point directly and no entrance slit was used in the optical system. As shown in Fig. 2, a Czerny–Turner configuration (Shafer *et al.*, 1964; Reader, 1969; Johnson *et al.*, 2009; Lee *et al.*, 2010) was adopted for beamline BL03U, which contains only three optical elements: two toroidal mirrors (M1 and M2) with a grazing-incidence angle of 7° and a planar grating with an including angle of 152°. Detailed parameters of the optical elements are summarized in Table 1. The incident light is collimated in both the horizontal and vertical direction by M1 and diffracted by the planar grating. The diffracted light is refocused on the exit slit by M2. Two gratings with line densities of 200 lines mm^{-1} (G1) and 400 lines mm^{-1} (G2) are used to cover the photon energy ranges 5–14 eV and 10–21 eV, respectively.

2.2. Gas filter

A gas filter was designed for the BL03U beamline to eliminate high-order harmonic radiation and maintain the other systems of the beamline in ultrahigh-vacuum environment. The gas filter, as shown in Fig. 3, is based on the concept at the VUV beamline (X04DB) at SLS (Johnson *et al.*, 2009) incorporating some adaptions and improvements. It consists of ten differentially pumped sections, and a series of apertures

Table 1
Optical elements of the beamline.

	M1	M2	G1	G2
Surface figure	Toroidal	Toroidal	Planar	Planar
Radius of curvature (mm)	R = 131288, ρ = 1950	R = 82055, ρ = 1219	–	–
Including angle (°)	166	166	152	152
Blank dimensions (mm)	100 × 30 × 30	200 × 30 × 30	100 × 30 × 30	100 × 30 × 30
Used area (mm)	90 × 15	180 × 15	90 × 15	90 × 15
Blank material	–	–	Silicon	Silicon
Coating	Au	Au	Au	Au
Groove density (lines mm^{-1})	–	–	200 (constant)	400 (constant)
Groove profile	–	–	Laminar, h = 160 nm, c/d = 0.6	Laminar, h = 85 nm, c/d = 0.6

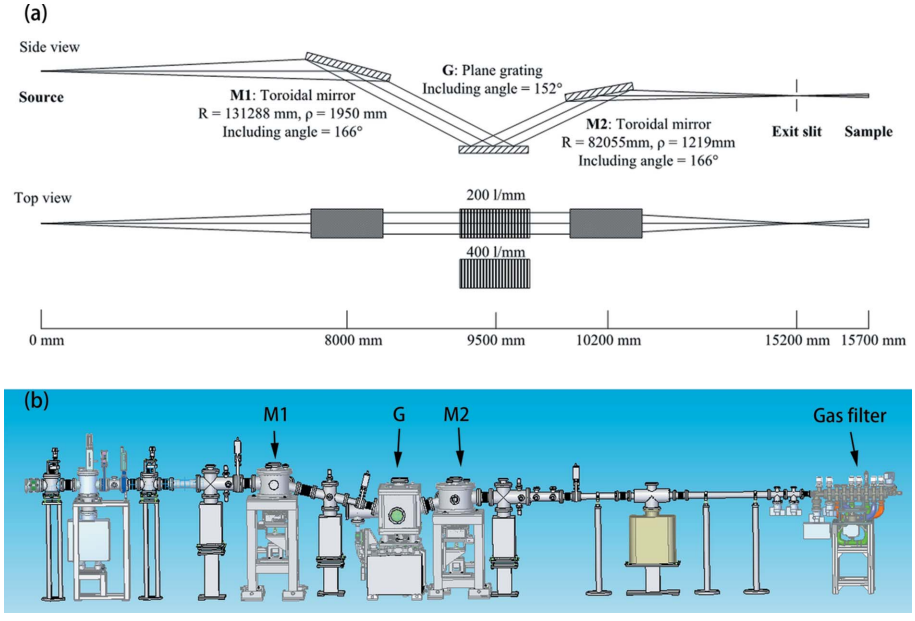

Figure 2
Schematic of the optical system (*a*) and layout of the beamline (*b*).

with rectangular openings are mounted between the adjacent sections. In order to obtain a small light spot at the endstations, the focal point of the monochromator is located in the center of section 8, rather than in the middle section. A stainless-steel sheet with six rectangular openings (height = 0.17, 0.20, 0.22, 0.25, 0.30, 0.50 mm, and width = 10 mm) was positioned at the center of section 8, acting as the exit slit of the beamline. The slit can be switched by a micrometer linear feedthrough according to the need of high photon flux or high energy resolution. The lengths of the four apertures between sections 1 and 5 are 10 mm, and those of the other apertures are 20 mm. The widths of the apertures are 2.8 mm, while the heights are 0.2 mm larger than the theoretical height of the local VUV light spot, which varies from 0.5 mm closest to the focal section to 1.8 mm between sections 1 and 2.

Noble gases (Ar, He or Ne) are filled into section 6 during the experiment, and the other sections are pumped by three 70 L s^{-1} turbopumps (sections 1, 2 and 10; Pfeiffer Vacuum, Hipace 80) and a Splitflow pump (Pfeiffer Vacuum, SplitFlow 310) with a high vacuum connection H (200 L s^{-1}, sections 3 and 9) as well as two intermediate connections: H1 (155 L s^{-1}, sections 4 and 8) and H2 (20 L s^{-1}, sections 5 and 7). The gas filter can be operated at pressures up to 1 kPa while the vacuum in section 1 is kept around 5 × 10^{-7} Pa. Actually, higher operating pressures can be acquired by decreasing the Splitflow pump to 50% of the full power while keeping the intermediate connection H2 closed. Table 2 lists the pressure distribution of the gas filter when filled with Ar and He. Moreover, as section 10 acts as a transfer stage between the gas filter and the endstations, the pressures in the endstations can be raised up to several Pascal without significant effect upon the vacuum in section 9. Moreover, hydrocarbon atoms produced from endstations are lethal for optics of the beamline, the gas filter can efficiently block hydrocarbon atoms from diffusing into the upstream of the beamline and avoid contamination of optics.

Fig. 4 shows the elimination efficiency for high harmonic radiation when the gas filter is filled with Ar. The elimination efficiency can be achieved at 99.97% when the pressure of the gas-inlet section is higher than 400 Pa.

2.3. Photon flux

The photon flux of the beamline was measured by an AXUV100 photodiode (International Radiation Detectors Inc.) mounted 600 mm behind the focus. The signal from the

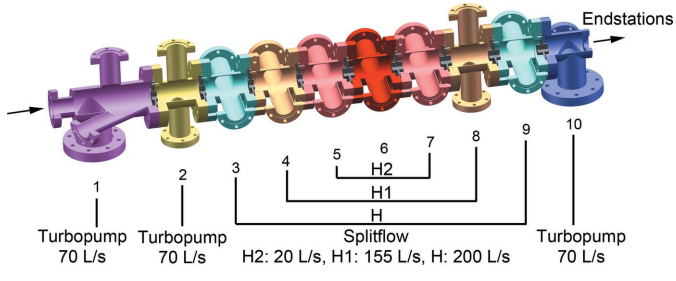

Figure 3
Schematic drawing of the gas filter.

Table 2
Pressure distribution of the gas filter when filled with Ar and He.

	Pressure (Pa)‡	
Section	Ar (200 sccm)	He (200 sccm)
1	5.0×10^{-7}	5.0×10^{-7}
3	4.6×10^{-1}	4.7×10^{-1}
4	5.2	4.7
5	5.7×10^{2}	1.5×10^{5}
6	6.1×10^{2}	1.5×10^{5}
7	5.5×10^{2}	1.5×10^{5}
10	4.2×10^{-1}	4.2×10^{-1}

‡ The Splitflow pump was decreased to 50% of the full power.

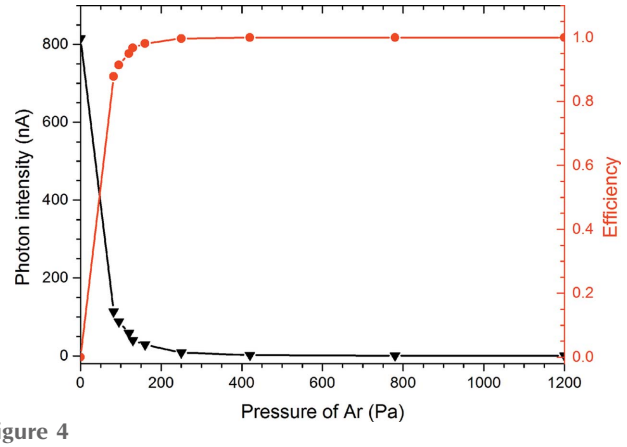

Figure 4
Elimination efficiency for high harmonic radiation *versus* the pressure of Ar in the gas filter.

photodiode was recorded by an electrometer (6517A, Keithley), and normalized with the responsivity curves. In order to filter the light from the high diffraction orders of the grating, the gas filter was filled with Ar for the 200 lines mm^{-1} grating and Ne for the 400 lines mm^{-1} grating, and the pressure of the gas-inlet section of the gas filter (section 6 in Fig. 3) was kept at 1000 Pa. The measurement was performed with a beam current of 300 mA. As shown in Fig. 5, with the 200 lines mm^{-1} grating, the photon flux of the beamline is higher than 1×10^{13} photons s^{-1} in the energy range 6–13 eV. The sharp drop near 11.8 eV is caused by the absorption of argon. For the 400 lines mm^{-1} grating, the photon flux is around (3–10) $\times$ 10^{12} photons s^{-1} in the energy range 11–21 eV. As the ionization energies of most organic molecules are in the energy range 6–12 eV, and the photoionization cross sections near threshold is relatively small (Cool, Wang *et al.*, 2005; Zhou *et al.*, 2009), high photon flux with the 200 lines mm^{-1} grating will facilitate the detection of trace compounds in flames, pyrolysis and oxidation processes.

2.4. Photon energy resolution

The energy resolution of the beamline was measured by the absorption spectra of the gas filter. Fig. 6 shows the krypton absorption spectra measured by the 200 lines mm^{-1} and 400 lines mm^{-1} gratings. The gas filter was filled with a mixture of neon and krypton with ratio of 70:1 at 770 Pa. Photons with

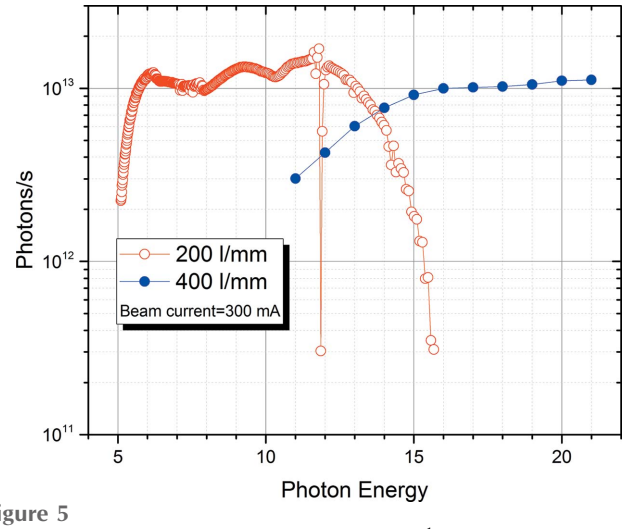

Figure 5
Measured photon flux for the 200 lines mm^{-1} grating (red) and the 400 lines mm^{-1} grating (blue).

energies higher than 21.6 eV were filtered out by neon. In order to calculate the energy resolution, the full width at half-maximum (FWHM) of the spectral line was obtained by Gaussian fitting. For the 200 lines mm^{-1} grating, as shown in Fig. 6(*a*), it is necessary to point out that the krypton absorption spectrum was measured at a diffraction order of m = +2. Thus the monochromator scanned over the energy range 7.15–7.35 eV while the gap of the undulator was set at the photon energy 14.3 eV.

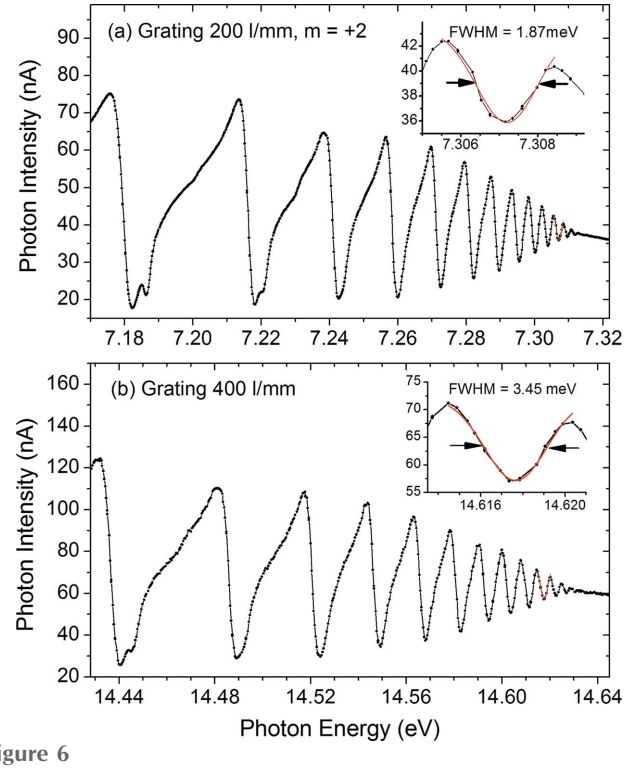

Figure 6
The krypton absorption showing the energy resolution of the 200 lines mm^{-1} grating (*a*) and the 400 lines mm^{-1} grating (*b*). The absorption spectrum for the 200 lines mm^{-1} grating is measured at the grating diffraction order of m = +2.

As shown by the insets of Fig. 6, the fitted FWHM is 1.87 meV at the monochromator energy of 7.3 eV for the 200 lines mm^{-1} grating, while the fitted FWHM is 3.45 meV at 14.6 eV for the 400 lines mm^{-1} grating. The energy-resolving power is 3900 at 7.3 eV for the 200 lines mm^{-1} grating and 4200 at 14.6 eV for the 400 lines mm^{-1} grating.

3. Combustion endstations

Combustion phenomena are basically chemical processes with rapid heat production. Tens of thousands of species and different types of reactions have to be considered for practical fuels like gasoline, kerosene and diesel. Laboratory-scale studies with state-of-the-art experimental approaches can provide comprehensive product identification and concentration information associated with the combustion process, making it possible to gain insights into the chemical kinetics of practical combustion (Kohse-Höinghaus *et al.*, 2005; Hansen *et al.*, 2009; Qi, 2013; Bierkandt *et al.*, 2015; Felsmann *et al.*, 2015). In particular, the applications of the synchrotron vacuum ultraviolet photoionization mass spectrometry (SVUV-PIMS) method have achieved a real leap forward in combustion diagnosis during the past ten years. The detections of some important intermediates like enols (Taatjes *et al.*, 2005), ketohydroperoxides (Battin-Leclerc *et al.*, 2010) and PAHs are contributing to uncovering the puzzles in auto-ignition and the formation of combustion pollutants, and opening the door to deeply exploring the combustion kinetics (Qi, 2013). However, some fascinating questions remain, especially concerning the measurements of some critically important radicals (*i.e.* H, O, OH, *etc.*), which generally have a rarely low concentration in standard combustion systems. Higher photon flux and specific endstation design may have the potential to be ground-breaking, uncovering new puzzles in the complicated chemistry of real fuel combustion. In this work, three types of experimental endstations based on the molecular beam mass spectrometry and single-photon ionization technique are designed for studies of premixed flames with McKenna burners, fuel pyrolysis in flow reactors and oxidation in jet-stirred reactors.

Fig. 7 presents sketches of the three endstations. Each endstation consists of a reactor chamber, an ionization chamber where the molecular beam intersects with the VUV light, and a reflectron time-of-flight (RTOF) mass spectrometer. A single-stage sampling interface is mounted between the reactor chamber and ionization chamber. The reactors with gas inlet system, the sampling interface and the time-of-flight mass spectrometer will be discussed in the following sections.

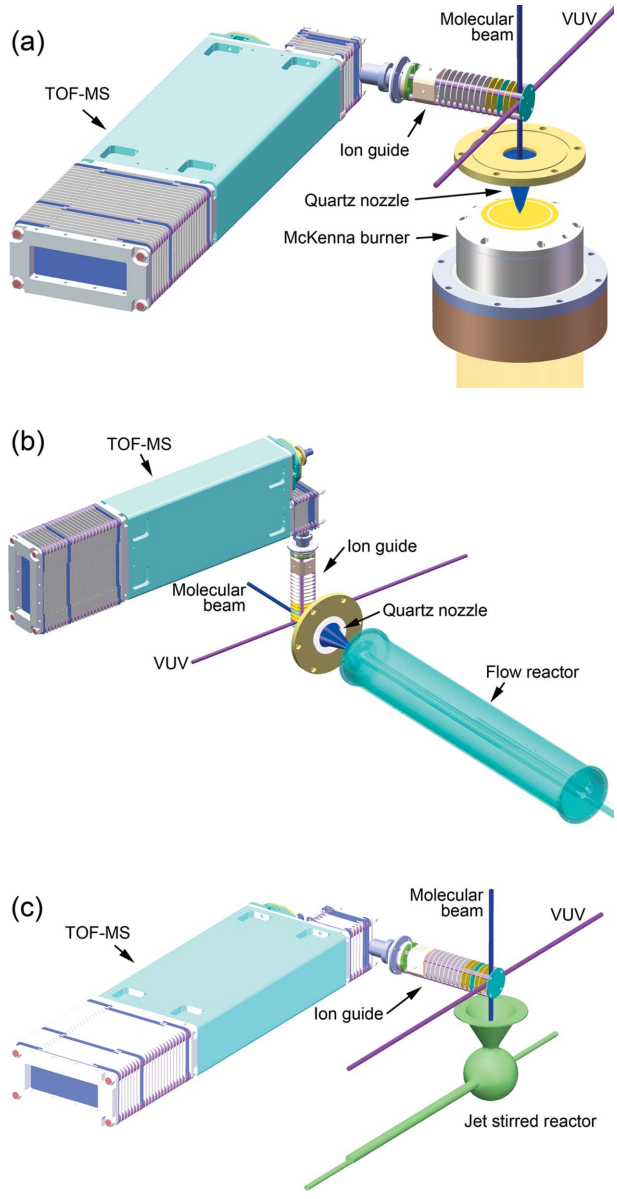

Figure 7
Sketches of the endstations for (*a*) premixed flame, (*b*) fuel pyrolysis in flow reactor and (*c*) oxidation in jet-stirred reactor. Each endstation is composed of a reactor chamber, an ionization chamber where the molecular beam intersects with the VUV light, and a time-of-flight mass spectrometer with a DC-only ion guide.

3.1. Reactors

Fig. 8(*a*) shows the assembly details of the chamber with McKenna burner. The burner is housed in a flame chamber with a diameter of 200 mm and a length of 400 mm and the pressure inside the flame chamber can be changed in the range 30–760 Torr. The translation of the burner is realised by a step motor (87000 Series, Haydon Linear Motors Co. Ltd).

The structure of the flame chamber has been improved to avoid fuel condensation. In the previous facility (Cool, McIlroy *et al.*, 2005; Qi *et al.*, 2006), the burner together with the translation rail are housed in the flame chamber. There is a 300 mm-long gas inlet pipe inside the chamber that cannot be heated and may cause condensation of liquid fuels. In this work, the burner is mounted at the end of a metal bellows, and the edge of the rear of the burner is used as the sealing surface. The whole gas-inlet pipe is positioned outside the flame chamber, and thus the whole pipe from the vaporizer to the burner can be heated for liquid fuels more conveniently.

Fig. 8(*b*) presents a sectional view of the flow reactor and temperature profiles along the centerline of the reactor. The flow reactor is composed of a home-made furnace and an α-type alumina ceramic tube with inner diameter of 7.0 mm and thickness of 1.5 mm. For the furnace, mounted in the center is a boron nitride tube with inner diameter of 11.0 mm, around which electrically heated wire is uniformly twined. The outermost layer of the furnace is a heat shield with thickness of about 32 mm. The ceramic tube is mounted coaxially with the furnace, and can be replaced easily without opening the furnace. A temperature-controlled tungsten–rhenium (W–Re) thermocouple is positioned close to the middle region of the reaction zone. The total length of the heating zone is about 60 cm. During the experiment, mixtures of argon and fuels in the gas phase are fed into the alumina tube, and the pyrolysis species are sampled 10 mm downstream from the outlet of the ceramic tube by a 30 mm-long quartz nozzle with a 25° cone angle.

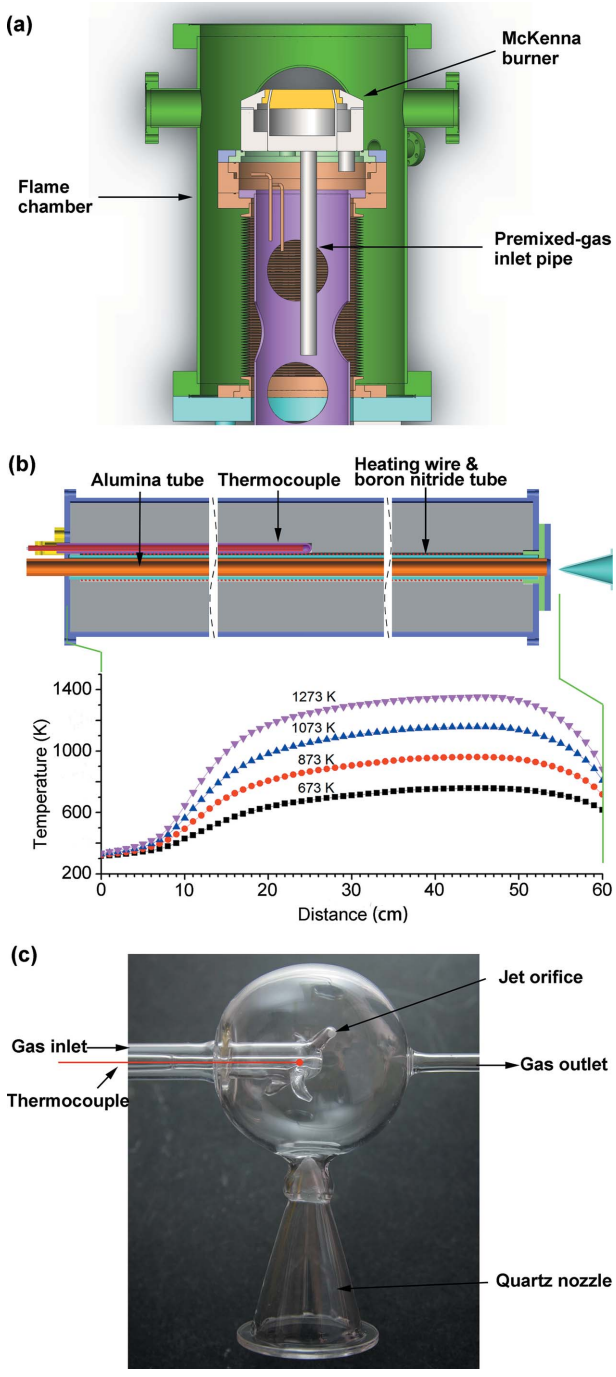

Figure 8
(*a*) Sectional view of the flame chamber with McKenna burner. (*b*) Sectional view of the flow reactor. (*c*) Photograph of the jet-stirred reactor showing details inside the spherical reactor and the connection with the quartz nozzle.

Temperature and pressure along the centreline of the reactor are key parameters in the pyrolysis experiments using flow reactor. The temperature calibration and pressure calculation have been reported in detail elsewhere (Zhang *et al.*, 2012). To ensure accuracy, temperature measurements were usually performed before and after each pyrolysis experiment.

Fig. 8(*c*) presents a sectional view and a photograph of the jet-stirred reactor. The inner diameter of the spherical reactor is 58 mm and the wall thickness is 2 mm. A quartz sampling nozzle with a ~70 µm orifice is welded into the sphere with the tip protruding several millimetres into the reactor. The gaseous reactants inside the reactor are well stirred with homogeneous concentration and temperature.

As the three endsations are mounted on a rail perpendicular to the beamline and only one endstation runs at a time, they share the same set of flow and pressure control system. The flow rates of gases (*e.g.* Ar, O_2, gas fuel) are controlled by mass flow controllers (MKS Instruments Inc.). For liquid fuels, a high-performance liquid chromagography (HPLC) pump (Zhengjinag Fuli Analytical Instruments Co. Ltd, China) is used to syringe the sample into a vaporizer. The reactor chamber is pumped with a single-stage rotary vane vacuum pump (SV100B, Leybold), and an MKS capacitance manometer is used to monitored the pressure of the reactor chamber. The pressure inside the reactor chamber is maintained automatically by a throttle valve.

3.2. Sampling interface

In the three endstations, conical quartz probes with included angle of 25° and thickness of ~1 mm are used as sampling nozzles. The diameter of the orifice is in the range 70–350 µm, depending on the pressure in the reactor required by different experiments. The wall thickness near the tip of the orifice was ground to less than 0.05 mm thickness to decrease the quenching of reactive species on the wall of the nozzle.

Another important design is shortening the distance between the sampling orifice of the quartz nozzle and ionization point, $D_{s\text{-}i}$. As the density of the molecular beam is inversely proportional to the square of the distance from the sampling orifice, a decreased $D_{s\text{-}i}$ will increase the density of sampled species and reduce the travel time, and thus enable the detection of more reactive species. In this work, a single-stage differentially pumped sampling interface is used. The molecular beam is extracted through a conical quartz nozzle into the ionization chamber directly. The ionization chamber is

pumped by a 1600 L s^{-1} turbomolecular pump, and the pressure was kept in the range 7×10^{-2} to 1×10^{-1} Pa during experiments. Compared with our previous flame machine, this kind of design features a $D_{s\text{-}i}$ of less than 100 mm.

3.3. Time-of-flight mass spectrometer

The TOF mass spectrometers of the three endstations are different to the one constructed at NSRL previously (Zhou *et al.*, 2013). The improvements include a simplified design of the TOF analyzer, as well as a significant simplification of the ion guide. As shown in Fig. 9(*a*), the mass spectrometer contains a DC-only ion guide and a modular-designed TOF analyzer. The voltages of the ion guide, ion extraction pulses and TOF analyzer, as well as the time sequence, are implemented by a home-made computer-controlled power supply [Fig. 9(*b*)].

The ion guide includes a set of einzel lenses, a DC quadrupole used for steering the ion beam and a set of slicer electrodes. The einzel lens consist of a 14-ring electrode stack of 1.0 mm-thick plates separated by 5.0 mm by polyetheretherketone washers. The first two electrodes in the stack have a constant 2.0 mm inner diameter, and the remaining 12 stainless steel electrodes have a constant 25.0 mm inner diameter, and no voltage divider is used. The DC-quad consists of four 15 mm-long rods of 6 mm diameter. The center of the rod lies on a 12.2 mm diameter and is fixed in place with a ceramic support.

The electrodes of the ion guide are powered by seven DC modules with ripple of less than 500 p.p.m. [DC Module for Ion Guide in Fig. 9(*b*)]. The total length of the ion guide is only 110 mm, which assists the transmission of ions. In our design, the ion guide acts as an intermediate stage between the ionization region and the TOF mass analyzer. The properties of the ion beam are optimized in terms of ion beam shape before the ions are injected into the extraction region of the TOF mass analyzer. As no RF optics are used, the energy of the ion beam is mainly controlled by the voltage drop from the first two electrodes to the slicer, and the energy dispersion cannot be compressed.

The operating cycle of the TOF mass analyzer has been described in detail elsewhere (Mamyrin *et al.*, 1973; Dodonov *et al.*, 2000; Guilhaus *et al.*, 2000; Zhou *et al.*, 2013). Briefly, as shown in Fig. 9(*c*), the first and third electrodes of the extraction region are connected with positive and negative pulses generated by the Dual Pulser part of the power supply, respectively, while the second one is kept at ground. A slice of the ion beam from the ion guide is accelerated into the acceleration column when the two pulses boost to high potential level simultaneously. The two pulses are triggered by a TTL signal from the Pulse/Delay Generator with a typical frequency of 30 kHz. Ions move through the acceleration column for further acceleration, and enter the field-free region floating at −2500 V. Later, the ions fly into the dual-stage ion mirror and back to the field-free region again, and finally hit the detector. The detector consists of an impedance-matched pair of microchannel plates in a chevron configuration. Each plate has a diameter of 25 mm with channel diameter of 6 µm and a 5.5° bias angle. A cone-shaped stainless steel anode positioned behind the second plate collects the electron current. The signals from the anode are amplified and directed to a multiscaler (FastComTec) triggered synchronously with the Dual Pulser. The internal discriminator of the multiscaler is used to eliminate the noise. Fig. 9(*d*) shows the time sequence of the TOF MS in a single operating cycle. Table 3 lists the parameters of the power supplies in detail. The jitter of the front edges of the high-voltage pulses generated by the

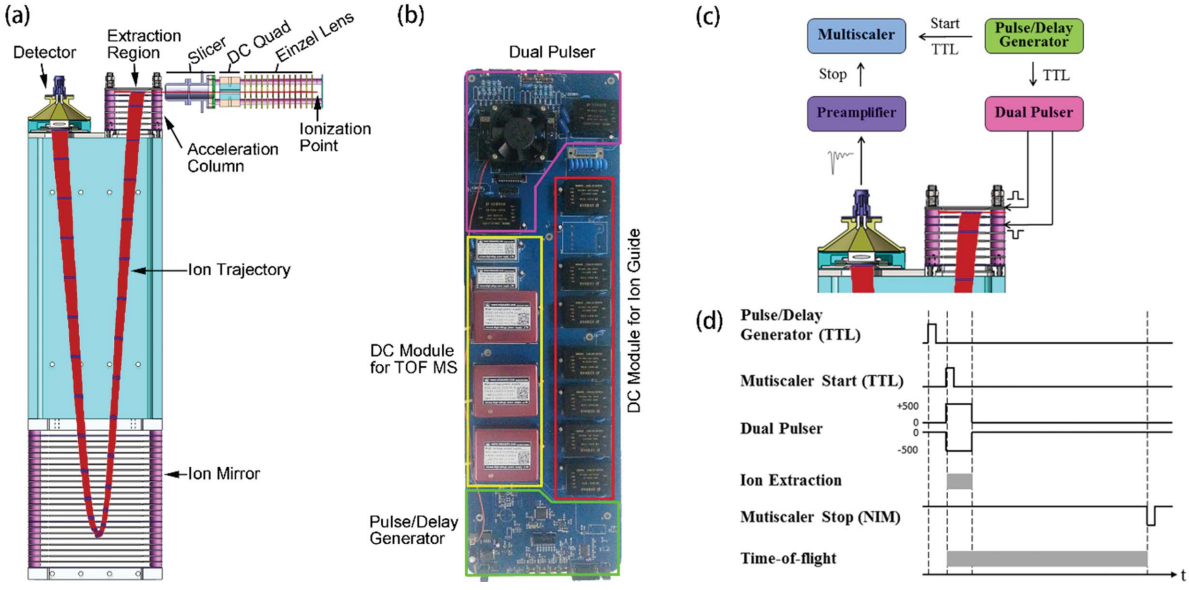

Figure 9
(*a*) Detailed drawing of the TOF MS showing the main components of the ion guide and the TOF mass analyser with simulated ion trajectory. (*b*) Photograph of the home-made integrated power supply showing the pulse/delay generator for time sequence control, the dual pulser for the ion extraction of the mass analyzer and DC modules for the ion guide and TOF MS. (*c*) Diagram of the triggering of the TOF MS. (*d*) Time sequence of the TOF MS.

Table 3
Key parameters of the power supplies.

DC module for ion guide	Voltage range	0 to +100 V 0 to −400 V
	Deviation	500 p.p.m./h 500 p.p.m./°C
	Ripple	<500 p.p.m.
Dual pulser module	Voltage range	0 to ±800 V
	Frequency range	1 to 50 kHz
	Front edge time	<10 ns
	Front edge jitter	<1 ns
DC module for TOF MS	Voltage range	0 to +2000 V 0 to −4000 V
	Deviation	10 p.p.m./h 10 p.p.m./°C
	Ripple	<10 p.p.m.

Dual Pulser is less than 1 ns, while the ripple of the DC module for TOF MS is less than 10 p.p.m. The software for the power supply and pulse/delay generator was developed in our laboratory.

4. Preliminary results

4.1. Mass resolution, limit of detection and signal stability

Fig. 10(*a*) presents a partial mass spectrum of gasoline, the inserts illustrate the obvious distinguishing of Ar and C_3H_4, and the FWHM at m/z = 92 is 0.044 Da, which indicates that the mass resolution is about 2100. The limit of detection (LOD) is also evaluated by detecting the CO_2 in argon-diluted air. Fig. 10(*b*) shows a plot of peak area *versus* the concentration of CO_2 in prepared gases, which indicates that the LOD is at the level of sub-p.p.m. with excellent linear response over the range from sub-p.p.m. to several percent.

The signal stability of the endstations over a long period is usually examined before data collection of each experiment. Fig. 10(*c*) shows that the variability of an individual peak is usually better than 5% for peaks with good signal-to-noise ratio.

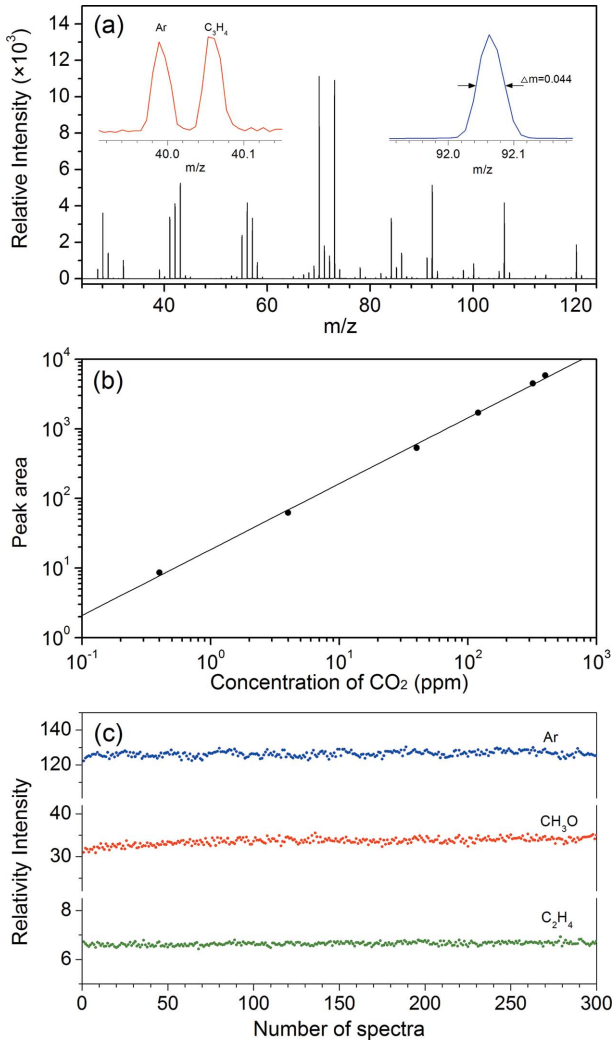

Figure 10
(*a*) Partial mass spectrum of gasoline obtained with a photon energy of 10.00 eV. (*b*) Limit of detection of the TOF MS. (*c*) Signal stability of three species in $C_2H_4/O_2/Ar$ flame during a period of 25 min; the recording time of each point is 5 s.

4.2. Reactive species in premixed flame

Most of the heat release in practical engines such as gasoline, diesel and gas turbines is produced by flames. Under flame conditions, the formation of pollutants such as nitrogen oxides (NOx), particulate matter (PM) and soot are a concern. In order to better control the emissions as well as increase the combustion efficiency, high-temperature oxidation mechanisms of hydrocarbon atoms and oxygenated fuels are demanded to reveal the combustion essence and perform accurate predictions for engine design. Detailed flame structure information can provide stringent constraints for the development of the combustion models (Egolfopoulos *et al.*, 2014). In this work, a premixed laminar $C_2H_4/O_2/Ar$ flame is used to illustrate the performance of the flame endstation. The flow rates of C_2H_4, O_2 and Ar are 0.229, 1.371 and 0.533 SLM (standard liters per minute), respectively. The pressure of the flame chamber is maintained at 30 Torr.

Fig. 11(*a*) shows a partial mass spectrum of the premixed $C_2H_4/O_2/Ar$ flame at a photon energy of 14 eV; the distance between the tip of the quartz nozzle and the burner surface was kept at 10 mm during data collection. Reactive species including H, O and OH can be clearly detected in this work, but they were not detected in previous premixed flame (Cool, McIlroy *et al.*, 2005; Qi *et al.*, 2006). Detecting these reactive species could be due to the following reasons: (i) the carefully ground orifice of the quartz nozzle reduces quenching of these reactive species, (ii) a shorter $D_{s\text{-}i}$ increases the density of these reactive species at the ionization point, and (iii) the photon flux from the new beamline is much higher than that used for combustion study previously ($\sim 5 \times 10^{10}$ photons s^{-1}) (Qi *et al.*, 2006). The photoionization efficiency spectra of H, O and OH shown in Figs. 11(*b*)–11(*d*) confirm the observation of the three reactive intermediates in the $C_2H_4/O_2/Ar$ flame. Because of the low concentrations and quenching during sampling, the detection of these important radicals is not easy

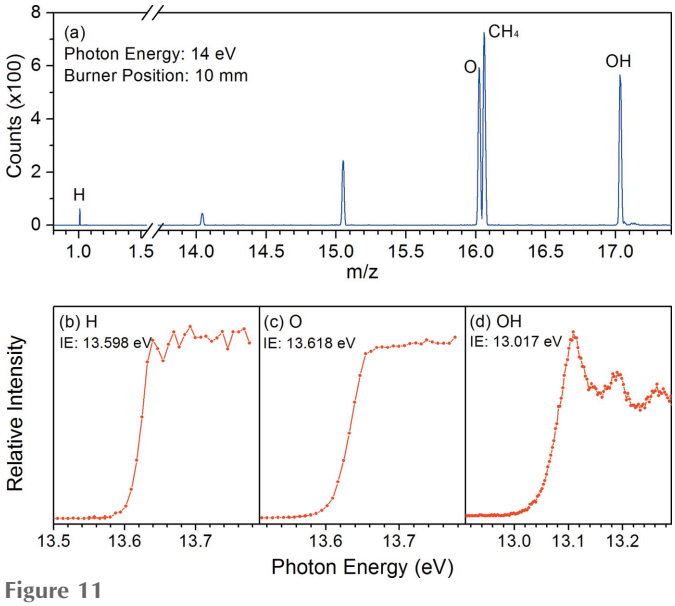

Figure 11
(*a*) Partial mass spectrum of $C_2H_4/O_2/Ar$ flame (the equivalence ratio φ = 0.5) showing the detection of H, O and OH at the burner position of 10 mm with 14 eV VUV light. (*b*)–(*d*) Photoionization efficiency spectra of H, O and OH.

(Lazzara *et al.*, 1973; Cole *et al.*, 1984; Bhargava & Westmoreland, 1998*a*,*b*; Law *et al.*, 2005; Cool *et al.*, 2007).

4.3. Pyrolysis of butanone in flow reactor

Pyrolysis is a critical part of the combustion process. Therefore, it is valuable to provide detailed information on the pyrolysis intermediates and develop pyrolysis mechanisms for hydrocarbon fuels (Westbrook *et al.*, 2009). In the experiment, a mixture of Ar and butanone is fed into an alumina flow tube in the center of the pyrolysis chamber. Ar is controlled by an MKS mass flow controller with a flow rate of 0.98 SLM while butanone is controlled by a HPLC pump with a liquid flow rate of 0.081 ml min^{-1} at room temperature. Butanone is vaporized and mixed with Ar in a vaporizer at 395 K. The pyrolysis species are sampled 10 mm downstream of the outlet by a quartz cone-like nozzle with a 25° cone angle and a 300 µm orifice at the tip. The pressure of the pyrolysis chamber is kept at 30 Torr during the experiment.

The mole fraction profiles of $C_2H_5COCH_3$, CO, CH_3, CH_2CO and CH_3CHCO are illustrated in Fig. 12. Butanone begins to decompose at around 950 K, and its concentration decreases gradually to full decomposition at 1350 K. The concentrations of CO and CH_3 increase continuously with increasing temperature, and the initial temperatures of the formation of CO and CH_3 are 1000 K and 950 K, respectively. The formation temperature of CH_2CO and CH_3CHCO is around 950 K. The maximum mole fractions of CH_2CO and CH_3CHCO are 1.0×10^{-3} and 1.8×10^{-3}, respectively.

4.4. Hydroperoxides during oxidation of *n*-butane in jet-stirred reactor

Concerning a needed reduction of the emission of greenhouse gases, understanding the auto-ignition chemistry of

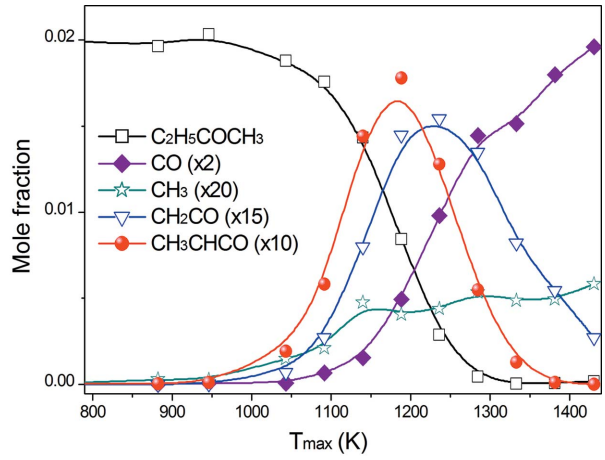

Figure 12
Mole fraction profiles of $C_2H_5COCH_3$, CO, CH_3, CH_2CO and CH_3CHCO as a function of heating temperature measured from butanone pyrolysis at 30 Torr.

hydrocarbon fuels and biofuels is of critical importance to allow the development of new combustion strategies for clean and efficient internal combustion engines (Lu *et al.*, 2011). Hydroperoxides (*R*OOH) are known to be the key species governing the first-stage ignition. The decomposition of the *R*O—OH bond of hydroperoxides is responsible for the degenerate branched-chain reactions and gives rise to the occurrence of auto-ignition. Due to the fragility of the *R*O—OH bond of hydroperoxides (the bond dissociation energy is around 43 kcal mol^{-1}), *R*OOH can easily break and is usually present in trace amounts, which can hardly be measured (Battin-Leclerc, 2008). The hydroperoxides formed during the low-temperature oxidation of *n*-butane were firstly observed by our previous facility (Battin-Leclerc *et al.*, 2010). In this work, the same experiment is repeated to test the performance of the new experimental setup. The experiment has been performed under quasi-atmospheric pressure, at a mean residence time of 6 s for a stoichiometric mixture of *n*-butane, oxygen and the carrier gas argon (composition = 4/26/70 in mol%).

Fig. 13(*a*) shows a mass spectrum with peaks of methylhydroperoxide (CH_3OOH), ethylhydroperoxide (C_2H_5OOH), butylhydroperoxide (C_4H_9OOH) and ketohydroperoxide ($C_4H_8O_3$) at m/z = 48, 62, 90 and 104, respectively. In order to confirm the observation, the photoionization efficiency spectra of the four species are obtained by integrating the spectra collected with different energies, as shown in Figs. 13(*b*)–13(*e*). The good agreement between the observed onsets with respective ionization energies in the literature (Battin-Leclerc *et al.*, 2010) clearly indicates the ability of tracing reactive hydroperoxides of the new facility.

5. Conclusion

The undulator-based VUV beamline BL03U has been constructed at NSRL mainly for combustion studies. The beamline delivers photons in the energy range 5–21 eV, with a photon flux of 10^{13} photons s^{-1} at 10 eV when the beam

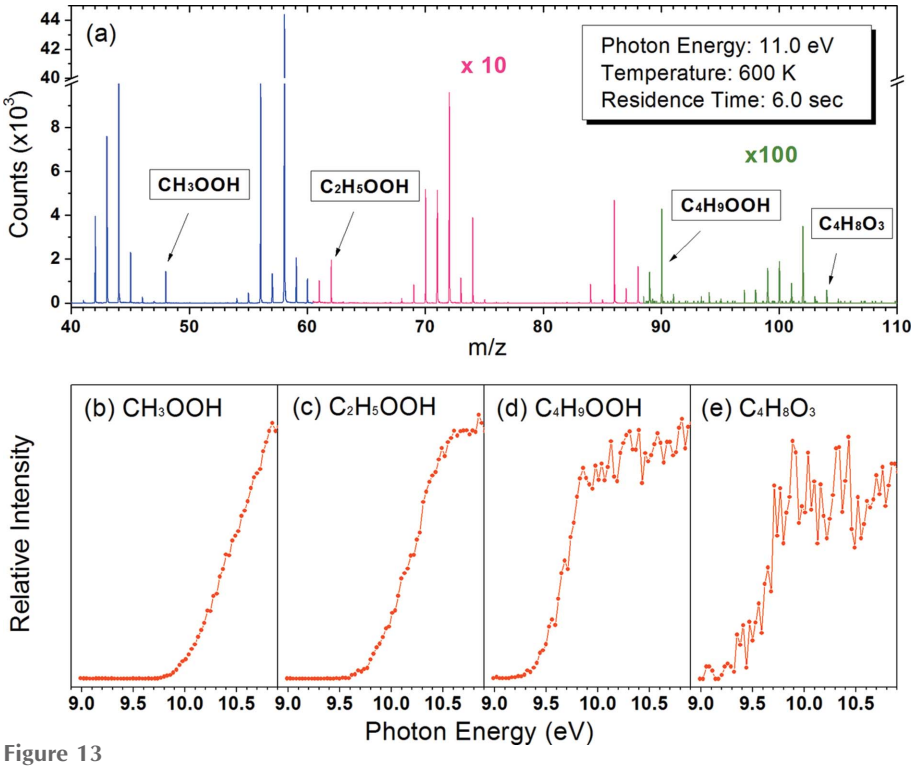

Figure 13
(*a*) Mass spectrum obtained for the oxidation of *n*-butane. (*b*)–(*e*) Photoionization efficiency spectra of CH_3OOH, C_2H_5OOH, C_4H_9OOH and $C_4H_8O_3$; the temperature inside the reactor is kept at 600 K.

current is 300 mA. The energy-resolving powers are measured at 3900 at 7.3 eV for the 200 lines mm^{-1} grating and 4200 at 14.6 eV for the 400 lines mm^{-1} grating. Three endstations have been designed for respective studies of premixed flames, fuel pyrolysis in flow reactors and oxidation in jet-stirred reactors. Each endstation contains a reactor chamber, an ionization chamber where the molecular beam intersects with the VUV light, and a home-made RTOF mass spectrometer. Some preliminary test results have also been presented, especially the ability of tracing reactive intermediates and radicals including H, O, OH and hydroperoxides. These results exhibit the advantage of the new VUV beamline and new endstations, as well as its potential contribution to other research topics.

Acknowledgements

The authors are grateful to Dr Thomas Gerber of Paul Scherrer Institut for providing the drawings of the gas filter. The work was supported by Natural Science Foundation of China (91541201, 11305175, U1332208), National Basic Research Program of China (973 Program) (2013CB834602) and Chinese Academy of Sciences.

References

Anderson, J. B. & Fenn, J. B. (1965). *Phys. Fluids*, **8**, 780–787.
Battin-Leclerc, F. (2008). *Prog. Energy Combust. Sci.* **34**, 440–498.
Battin-Leclerc, F., Herbinet, O., Glaude, P.-A., Fournet, R., Zhou, Z. Y., Deng, L. L., Guo, H. J., Xie, M. F. & Qi, F. (2010). *Angew. Chem. Int. Ed.* **49**, 3169–3172.
Bhargava, A. & Westmoreland, P. R. (1998*a*). *Combust. Flame*, **113**, 333–347.
Bhargava, A. & Westmoreland, P. R. (1998*b*). *Combust. Flame*, **115**, 456–467.
Bierkandt, T., Kasper, T., Akyildiz, E., Lucassen, A., Oßwald, P., Köhler, M. & Hemberger, P. (2015). *Proc. Combust. Inst.* **35**, 803–811.
Buckmaster, J., Clavin, P., Liñán, A., Matalon, M., Peters, N., Sivashinsky, G. & Williams, F. A. (2005). *Proc. Combust. Inst.* **30**, 1–19.
Campargue, R. (1984). *J. Phys. Chem.* **88**, 4466–4474.
Cole, J. A., Bittner, J. D., Longwell, J. P. & Howard, J. B. (1984). *Combust. Flame*, **56**, 51–70.
Cool, T. A., McIlroy, A., Qi, F., Westmoreland, P. R., Poisson, L., Peterka, D. S. & Ahmed, M. (2005). *Rev. Sci. Instrum.* **76**, 094102.
Cool, T. A., Wang, J., Hansen, N., Westmoreland, P. R., Dryer, F. L., Zhao, Z., Kazakov, A., Kasper, T. & Kohse-Höinghaus, K. (2007). *Proc. Combust. Inst.* **31**, 285–293.
Cool, T. A., Wang, J., Nakajima, K., Taatjes, C. A. & Mcllroy, A. (2005). *Int. J. Mass Spectrom.* **247**, 18–27.
Dodonov, A. F., Kozlovski, V., Soulimenkov, I., Raznikov, V., Loboda, A., Zhen, Z., Horwath, T. & Wollnik, H. (2000). *Eur. J. Mass Spectrom.* **6**, 481–490.
Egolfopoulos, F. N., Hansen, N., Ju, Y., Kohse-Höinghaus, K., Law, C. K. & Qi, F. (2014). *Prog. Energy Combust. Sci.* **43**, 36–67.
Emmons, H. W. (1971). *Symposium (Int.) Combust.* **13**, 1–18.
Felsmann, D., Moshammer, K., Krüger, J., Lackner, A., Brockhinke, A., Kasper, T., Bierkandt, T., Akyildiz, E., Hansen, N., Lucassen, A., Oßwald, P., Köhler, M., Garcia, G. A., Nahon, L., Hemberger, P., Bodi, A., Gerber, T. & Kohse-Höinghaus, K. (2015). *Proc. Combust. Inst.* **35**, 779–786.
Guan, Q., Urness, K. N., Ormond, T. K., David, D. E., Barney Ellison, G. & Daily, J. W. (2014). *Int. Rev. Phys. Chem.* **33**, 447–487.
Guilhaus, M., Selby, D. & Mlynski, V. (2000). *Mass Spectrom. Rev.* **19**, 65–107.
Hansen, N., Cool, T. A., Westmoreland, P. R. & Kohse-Höinghaus, K. (2009). *Prog. Energy Combust. Sci.* **35**, 168–191.
Heimann, P. A., Koike, M., Hsu, C. W., Blank, D., Yang, X. M., Suits, A. G., Lee, Y. T., Evans, M., Ng, C. Y., Flaim, C. & Padmore, H. A. (1997). *Rev. Sci. Instrum.* **68**, 1945–1951.
Hemberger, P., Trevitt, A. J., Gerber, T., Ross, E. & da Silva, G. (2014). *J. Phys. Chem. A*, **118**, 3593–3604.
Hwang, C. S., Chang, C. H., Lin, F. Y., Chen, H. H., Fan, T. C., Wang, C., Chang, H. P., Chen, J. & Hsu, K. T. (2002). *Rev. Sci. Instrum.* **73**, 1436–1439.
Johnson, M., Bodi, A., Schulz, L. & Gerber, T. (2009). *Nucl. Instrum. Methods Phys. Res. A*, **610**, 597–603.
Kantrowitz, A. & Grey, J. (1951). *Rev. Sci. Instrum.* **22**, 328–332.
Kohse-Höinghaus, K., Barlow, R. S., Aldén, M. & Wolfrum, J. (2005). *Proc. Combust. Inst.* **30**, 89–123.
Krüger, J., Garcia, G. A., Felsmann, D., Moshammer, K., Lackner, A., Brockhinke, A., Nahon, L. & Kohse-Höinghaus, K. (2014). *Phys. Chem. Chem. Phys.* **16**, 22791–22804.
Law, M. E., Carrière, T. & Westmoreland, P. R. (2005). *Proc. Combust. Inst.* **30**, 1353–1361.

Lazzara, C. P., Biordi, J. C. & Papp, J. F. (1973). *Combust. Flame*, **21**, 371–382.
Lee, K.-S., Thompson, K. P. & Rolland, J. P. (2010). *Opt. Express*, **18**, 23378–23384.
Linstrom, P. J. & Mallard, W. G. (2016). *NIST Chemistry WebBook*, http://webbook.nist.gov/chemistry/.
Lu, X., Han, D. & Huang, Z. (2011). *Prog. Energy Combust. Sci.* **37**, 741–783.
Mamyrin, B. A., Karataev, V. I., Shmikk, D. V. & Zagulin, V. A. (1973). *Sov. Phys. JETP*, **37**, 45.
Miller, J. A., Pilling, M. J. & Troe, J. (2005). *Proc. Combust. Inst.* **30**, 43–88.
Nahon, L. & Alcaraz, C. (2004). *Appl. Opt.* **43**, 1024–1037.
Nahon, L., de Oliveira, N., Garcia, G. A., Gil, J.-F., Pilette, B., Marcouillé, O., Lagarde, B. & Polack, F. (2012). *J. Synchrotron Rad.* **19**, 508–520.
Oßwald, P., Hemberger, P., Bierkandt, T., Akyildiz, E., Köhler, M., Bodi, A., Gerber, T. & Kasper, T. (2014). *Rev. Sci. Instrum.* **85**, 025101.
Photoionization Cross Section Database (2011). Photoionization Cross Section Database, Version 1.0, http://flame.nsrl.ustc.edu.cn/en/database.htm.
Qi, F. (2013). *Proc. Combust. Inst.* **34**, 33–63.
Qi, F. & McIlroy, A. (2005). *Combust. Sci. Technol.* **177**, 2021–2037.
Qi, F., Yang, R., Yang, B., Huang, C. Q., Wei, L. X., Wang, J., Sheng, L. S. & Zhang, Y. W. (2006). *Rev. Sci. Instrum.* **77**, 084101.
Reader, J. (1969). *J. Opt. Soc. Am.* **59**, 1189–1196.
Shafer, A. B., Megill, L. R. & Droppleman, L. (1964). *J. Opt. Soc. Am.* **54**, 879–887.
Smalley, R. E., Wharton, L. & Levy, D. H. (1977). *Acc. Chem. Res.* **10**, 139–145.
Taatjes, C. A., Hansen, N., McIlroy, A., Miller, J. A., Senosiain, J. P., Klippenstein, S. J., Qi, F., Sheng, L. S., Zhang, Y. W., Cool, T. A., Wang, J., Westmoreland, P. R., Law, M. E., Kasper, T. & Kohse-Höinghaus, K. (2005). *Science*, **308**, 1887–1889.
Westbrook, C. K., Mizobuchi, Y., Poinsot, T. J., Smith, P. J. & Warnatz, J. (2005). *Proc. Combust. Inst.* **30**, 125–157.
Westbrook, C. K., Pitz, W. J., Herbinet, O., Curran, H. J. & Silke, E. J. (2009). *Combust. Flame*, **156**, 181–199.
Yang, Y.-F., Lu, H.-H., Chen, W., Jia, Q.-K., Sun, S.-C. & Li, Z.-Q. (2014). *Chin. Phys. C*, **38**, 077002.
Zhan, D., Rose, J. & Fenn, J. B. (1998). *J. Am. Soc. Mass Spectrom.* **9**, 1241–1247.
Zhang, Y. J., Cai, J. H., Zhao, L., Yang, J. Z., Jin, H. F., Cheng, Z. J., Li, Y. Y., Zhang, L. D. & Qi, F. (2012). *Combust. Flame*, **159**, 905–917.
Zhou, Z., Xie, M., Wang, Z. & Qi, F. (2009). *Rapid Commun. Mass Spectrom.* **23**, 3994–4002.
Zhou, Z. Y., Wang, Y., Tang, X. F., Wu, W. H. & Qi, F. (2013). *Rev. Sci. Instrum.* **84**, 014101.